# Design and Implementation of Analog-Digital Hybrid Beam-Formers for Low-Complexity Ultrasound Systems: A Feasibility Study

Heechul Yoon , Junseung Kim , Tai-kyong Song *

Posted Date: 23 October 2023

doi: 10.20944/preprints202310.1453.v1

Keywords: analog beamforming; hybrid beamforming systems; point-of-care ultrasound; wearable ultrasound; massive-channel systems; ultrasound system design

*Article*

# Design and Implementation of Analog-Digital Hybrid BeamFormers for Low-Complexity Ultrasound Systems: A Feasibility Study

**Heechul Yoon [1], Junseung Kim [2] and Tai-kyong Song [2,*]**

[1] School of Electronics and Electrical Engineering, Dankook University, Yongin-si, Republic of Korea; heechul.yoon@dankook.ac.kr

[2] Department of Electronic Engineering, Sogang University, Seoul, Republic of Korea

* Correspondence: tksong@sogang.ac.kr; Tel.: +82-2-705-8907

**Abstract:** Low-complexity ultrasound systems are increasingly desired for both wearable, point-of-care ultrasound and high-end massive-channel ultrasound for 3-D matrix imaging. However, the imaging capabilities, including spatial resolution and contrast, could suffer, as the low complexity systems are pursued, which remains as an unresolved tradeoff. To mitigate this limitation, this study revisits the general structures of analog and digital beamformers and introduces a hybrid approach, referred to as analog-digital hybrid beamforming, to implement efficient ultrasound systems. The suggested hybrid beamforming takes two stages sequentially, where the first analog stage partially beamforms *M*-channel RF signals to *N* sum-out data (i.e., *M*-to-*N* beamforming), and the second digital stage beamforms *N* partial sums to single final beamformed data (i.e., *N*-to-1 beamforming). Our approach was systematically designed and implemented with only four major integrated circuits, which was capable of driving full 64-channel transmission and reception. The developed system was demonstrated with a customized 64-channel 1-D phased array using a commercial tissue mimicking phantom. From the phantom imaging results, signal-to-noise ratio, contrast-to-noise ratio, and full beam width at half maximum values were quantitatively evaluated. The demonstrated results indicate that the analog-digital hybrid beamforming can be applied to any type of arrays for either sophisticated 3-D imaging and tiny wearable ultrasound applications.

**Keywords:** analog beamforming; hybrid beamforming systems; point-of-care ultrasound; wearable ultrasound; massive-channel systems; ultrasound system design

## 1. Introduction

Medical ultrasound imaging has been one of the essential screening and diagnostic tools in the clinic with a wide range of system families from wearable, portable point-of-care ultrasound (POCUS) to high-end sophisticated machines. Wearable ultrasound and POCUS have been increasingly used, as they are relatively easy-to-learn, accessible to patients, and versatile as a diagnostic tool [1, 2]. Moreover, due to recent technical advances, ultrasound systems have become more functional, capable of offering acoustic, biomechanical, and optical properties of complex pathologies in real-time [3-5]. Therefore, clinical utility of ultrasound also has expanded; in addition to cardiac and thoracic applications, POCUS can be useful to patients with dyspnea, hemodialysis, pneumonia, and ventricular dysfunction [6].

The diagnostic capabilities of ultrasound imaging with wearable ultrasound, POCUS, and even high-end machines basically rely on spatial resolution and contrast of the image [7, 8]. However, ultrasound waves diffract along the propagation, and thus, the resolution of ultrasound is only favorable near the focus [9]. This limitation because of wave diffraction in imaging resolution has been continuously improved with digital techniques, including dynamic receive beamforming [10-12]. Synthetic aperture ultrasound, ultrasound localization microscopy, referred to as super-resolution ultrasound, and many other approaches reducing the level of sidelobe, and the beam width of main lobe have been investigated to enhance the spatial resolution [13-16].

 doi:10.20944/preprints202310.1453.v1



This fundamental limitation on the spatial resolution of ultrasound is associated with electrical focusing of an array transducer; an array with a larger dimension with the greater number of active channels for transmit/receive operations can improve the spatial resolution in general [17]. For this electrical focusing, digital beamforming is most typically used in modern ultrasound scanners, which desire one analog-to-digital converter (ADC) and one digital first-in-first-out (FIFO) memory per receiving channel [11]. Therefore, the greater number of channels linearly increases the system complexity and thus the production cost. This would be critical not only for a small, handheld device for wearable ultrasound and POCUS, but also for high-end ultrasound supporting 3-D imaging applications [18-20]. Recent progressive utilization of a 2-D matrix array necessitates one-to-one connection of every array element and system channel, which is often a major concern in its practical implementation. For example, a 32 × 32 2-D matrix array simply requires 1,024 channels with the same number of pulsers and receivers [18]. Thus, to reduce the active number of channels in 3-D imaging, sparse arrays and row-column addressed arrays are often considered, but at the expense of the image quality [21-23].

Adopting analog beamforming or analog-digital hybrid beamforming approaches could help reduce the amount of system components [24]. As the analog beamformer sums out receiving analog signals without digitization, it does not use ADCs and digital FIFOs for every channel but uses the analog FIFO simply consisting of one capacitor per FIFO cell [25, 26]. However, every cell in the analog FIFO should be precisely time-controlled for dynamic receive beamforming and data loss could occur over time due to capacitor discharging. Thus, when the time delay differences between receiving channels are long, the data loss could become more problematic.

Analog-digital hybrid beamformers could overcome these respective downsides of both analog and digital beamformers [27]. To mitigate the data discharging problem in the analog FIFO cell and to leverage the system complexity, this study investigates a two-stage analog-digital hybrid beamformer architecture and its systematic implementation. The first analog part of the beamformer focuses the *M*-channel receiving signals to *N* partial sum out signals (i.e., *M*-to-*N* beamforming), which are digitized for the second digital beamforming stage. The second digital part beamforms *N* signals to one final sum out (i.e., *N*-to-1 beamforming). Design and implementation of our two-stage analog-digital hybrid beamforming approach with phantom imaging results are presented using a customized 1-D phased array, but the same principles validated in this study can be applied to any type of arrays, including a 2-D array transducer with the greater number of channels in general.

## 2. Materials and Methods

### *2.1. Digital and Analog Beamformers*

Figure 1 illustrates digital and analog beamformer structures. As shown in Figure 1 (a), a digital beamformer generally comprises an ADC and a digital FIFO per receiving channel and a digital adder for final summation of all delayed signals [11, 12]. For the digital beamformer, all receiving echoes are stored in every digital FIFO synchronously and simultaneously, which are read out at different variable times, depending on the time delays required for coherent summation [10]. The digital beamformer is expected to be precise in beamforming and once the RF data is sampled and stored in the FIFO, the data would be stably utilized for beamforming. However, because one ADC is required for individual receiving channel for digital beamformers, the system complexity and associated power consumption linearly increase with respect to the number of channels.

Preprints (www.preprints.org) | NOT PEER-REVIEWED | Posted: 23 October 2023 doi:10.20944/preprints202310.1453.v1



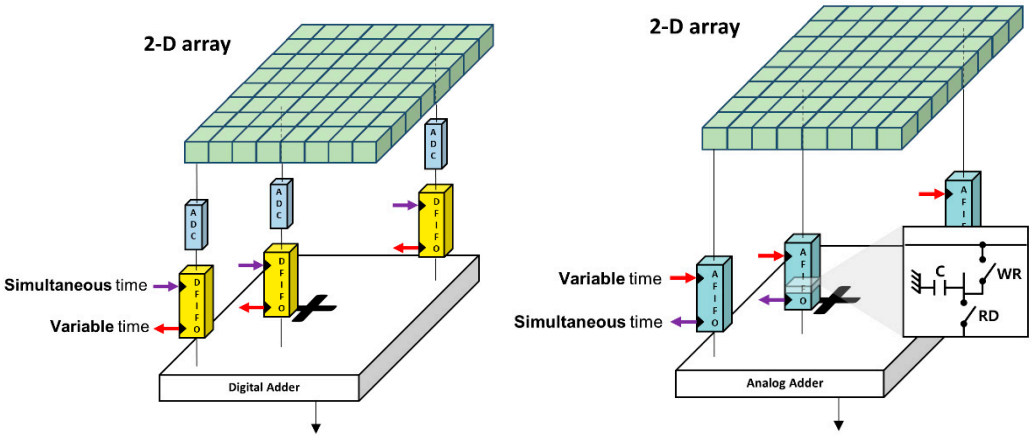


(a) (b)

**Figure 1.** General structures of (**a**) digital and (**b**) analog beamformers. A digital beamformer generally consists of an ADC and a digital FIFO for every channel, followed by a digital adder for final beamformation, and an analog beamformer does not have ADCs, but uses analog FIFOs comprising a single capacitor and two switches for read/write operations per receiving channel, followed by an analog adder.

Analog beamformers, as shown in Figure 1 (b), could resolve the challenges in digital beamformers, but have other limitations. Each cell in the analog FIFO has two switches controlling write and read operations of received analog signals and a capacitor for their storage [26]. In contrast to digital beamformers, analog beamformers apply focusing delays prior to deposition of the data into the FIFO. Thus, receiving ultrasound echoes are stored at variable different times along the analog FIFO cells, depending on the time delays for beamforming based on a sample-and-hold approach. For the final beam formation, the stored data is read out simultaneously, possibly followed by simple wired addition. Although analog beamformers can make the imaging systems more efficient, the data loss in the cells would be a matter. The amount of data loss between channels can vary because of focusing delays, which could cause nonuniform signal strengths between channels. Furthermore, the number of taps (or cells) of analog FIFO determines the longest focusing delays between channels, limiting the utility of the imaging systems.

### *2.2. Analog-Digital Hybrid Beamformer*

An analog-digital hybrid beamformer could leverage respective limitations in analog and digital beamformers [28]. As shown in Figure 2, given an $M$-channel array transducer, $N$ analog beamformers first partially focus analog RF data and output $N$ partial sum data (i.e., $M$-to-$N$ analog beamforming), which is sampled through ADCs and digitally beamformed (i.e., $N$-to-1 digital beamforming), producing a single sum-out result. In the $M$-to-$N$ analog beamforming stage, a total of $M$ channels is grouped into $N$ sub-aperture groups. Thus, each analog beamformer takes $M/N$ channels of RF data and produces $N$ partial sums, followed by the $N$-to-1 digital beamforming process.

Preprints (www.preprints.org) | NOT PEER-REVIEWED | Posted: 23 October 2023 doi:10.20944/preprints202310.1453.v1



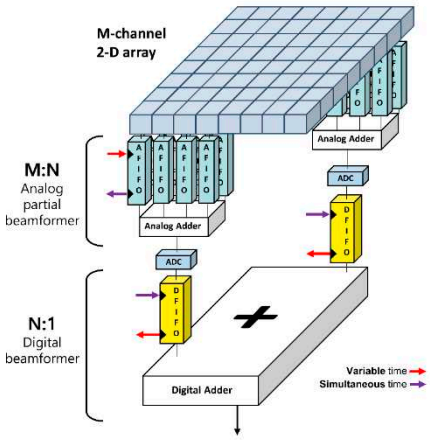


**Figure 2.** Analog-digital hybrid beamformer for massive-channel ultrasound systems. Any type of arrays with $M$ number of elements beamform the first analog signals, producing $N$ partially beamformed signals, which are digitized for the second digital beamforming for final delay-and-sum.

Figure 3 shows the block diagram of the analog-digital hybrid beamforming system. Each cell, referred to also as a tap, in the analog FIFO is again consisted of a single capacitor with two write/read switches. These taps (or cells) are serially connected to support continuous storing of the receiving signals and their beamforming, which is controlled by the sampling clock generator with variable write and simultaneous read timing signals. Partial analog sums of $N$ analog partial beamformers are sampled with $N$ ADCs and digitally beamformed at the end.

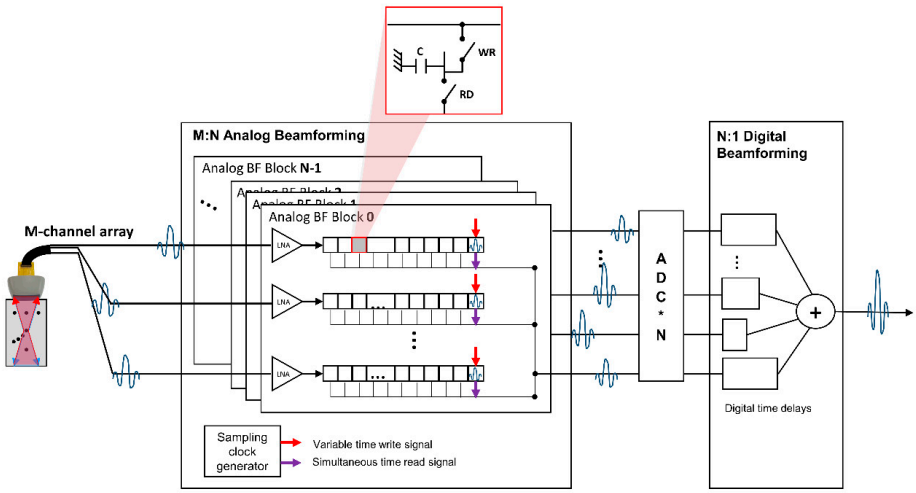


**Figure 3.** System block diagram of an analog-digital hybrid beamformer with a $M$-channel array transducer. The analog beamforming part produces $N$ beamformed signals from $M$ receiving RF data, which are sampled then by $N$ ADCs for the last N-to-1 digital beamforming. Here, the sampling clock generator controls the data charging timing of each capacitor in the serial taps in the analog FIFO.

Geometric representation of a 2-D array transducer and delay calculation for partial analog beamforming are described in Figure 4. The general 2-D array with $M$ elements is assumed to be located at the x-y plane, as shown in Figure 4 (a). The positions of each array element and the imaging target are represented by $E_i(x_i, y_i, 0)$ and $U_k(x_k, y_k, z_k)$, respectively, in the 3-D coordinate system. Here, the index $i$ represents individual elements ranging from 1 to $M$ and the index $k$ represents the imaging points. $\theta$ and $\varphi$ are polar and azimuthal angles defining the scanning direction. $R$

Preprints (www.preprints.org) | NOT PEER-REVIEWED | Posted: 23 October 2023 doi:10.20944/preprints202310.1453.v1



represents the distance between the array origin and the imaging point of interest. The two-way round-trip time-of-flight $\tau(E_i, U_k)$ can then be defined as follows.

$$\tau(E_i, U_k) = \left( R + \sqrt{(x_k - x_i)^2 + (y_k - y_i)^2 + z_k^2} \right) / c \quad (1)$$

where $c$ represents the speed of sound. Considering receiving delays for a sub-group with $M/N$ channels, as described in Figure 4 (b), the number of taps of analog FIFOs should support the maximum and minimum delays required within a sub-group, as the sub-group elements continuously receive and store the analog data for beamforming. Specifically, defining the sample-and-hold time of each tap as $T_s$, also referred to as a tap charging time, a maximum delay difference within the sub-grouped elements should satisfy the following condition.

$$max\big(\tau(E_i, U_k)\big) - min\big(\tau(E_i, U_k)\big) \leq \#\ taps\ \times\ T_s \quad (2)$$

The condition in Equation (2) guarantees that partial summation of analog part of the beamformer can rely on the receiving RF data from the current target-of-interest. If this condition is not satisfied, the data received from the different locations can be undesirably mixed during beam formation. Every subgroup of partial analog beamforming should satisfy Equation (2).

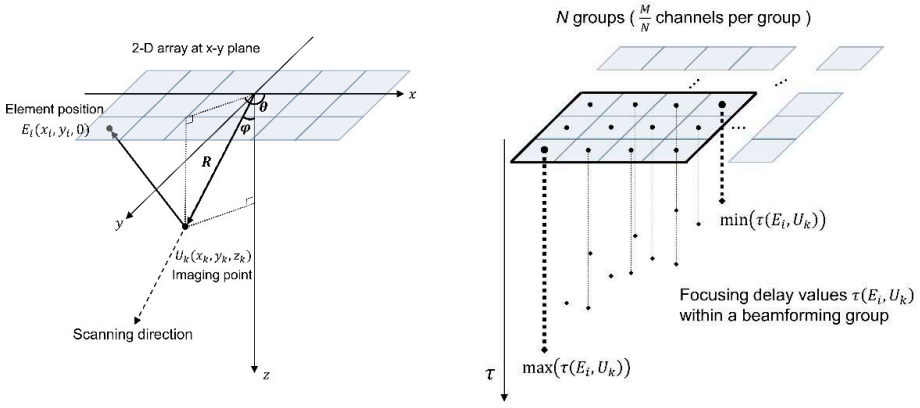


(a) (b)

**Figure 4.** (**a**) Geometrical representation of a general 2-D array in the 3-D space and (**b**) receiving delay calculation with a sub-group of 2-D array. Scanning direction is defined with polar and azimuthal angles (i.e., $\theta$ and $\varphi$) and the imaging point-of-interest is defined as $U_k(x_k, y_k, z_k)$ in (a). Given sub-groups of partial analog beamforming in (b), the maximum and the minimum receiving time delays should be within the limit of the analog beamformer, which is determined by the number of the tabs (or cells) in the analog FIFO.

### *2.3. Design and Implementation of Analog-Digital Hybrid Beamforming System*

Figure 5 shows the functional block diagram of our analog-digital hybrid beamforming system, consisting of a field programmable gate array (FPGA), analog front-end (AFE) integrated circuits (ICs), and a microcontroller unit (MCU). For the AFE part, US7502 (ABLIC, Inc., Tokyo, Japan) was used for 64-channel transmission and 64-to-8 partial analog beamforming. The 8-channel analog beamformed data from the US7502 IC is digitized through a single AFE IC with 8-channel ADCs (AFE5801, Texas Instruments, Dallas, Texas, USA) and then transferred to the FPGA (Artix-7 XC7A200T, Xilinx, Inc., San Jose, California, USA) through low-voltage differential signaling (LVDS) for digital beamforming and signal processing. To provide a user application with the system, a tablet host device (Galaxy S6, Samsung Electronics Co., Ltd, Suwon-si, Republic of Korea) and the developed system are interfaced via universal serial bus (USB) communication through the bridge MCU (CYUSB3014-BZXI, Infineon Technologies AG, Neubiberg, Germany). Thus, only four major ICs (two AFE ICs, one FPGA, and one MCU) are used to design an ultrasound imaging system capable of full 64-channel driven transmission and reception.

Preprints (www.preprints.org) | NOT PEER-REVIEWED | Posted: 23 October 2023 doi:10.20944/preprints202310.1453.v1



The post-beamformed RF data processed in the FPGA is demodulated to provide the IQ data, which was transferred to the host device for further signal and image processing to reconstruct B-mode ultrasound images in real time. From the IQ data, the envelope of the signal was first extracted and then log-transformed to adjust the dynamic range of the signals. Digital time gain compensation along the depth was applied to the log-transformed data to recover the attenuated intensity of the signals. A simple 3 by 3 median filtering was applied to fill the black holes in the gain compensated data to mitigate the speckle noises. A final signal processing step in the host device is the digital scan conversion, which reformats the image to display a sector form of the images obtained by the phased array steering from –45° to +45°.

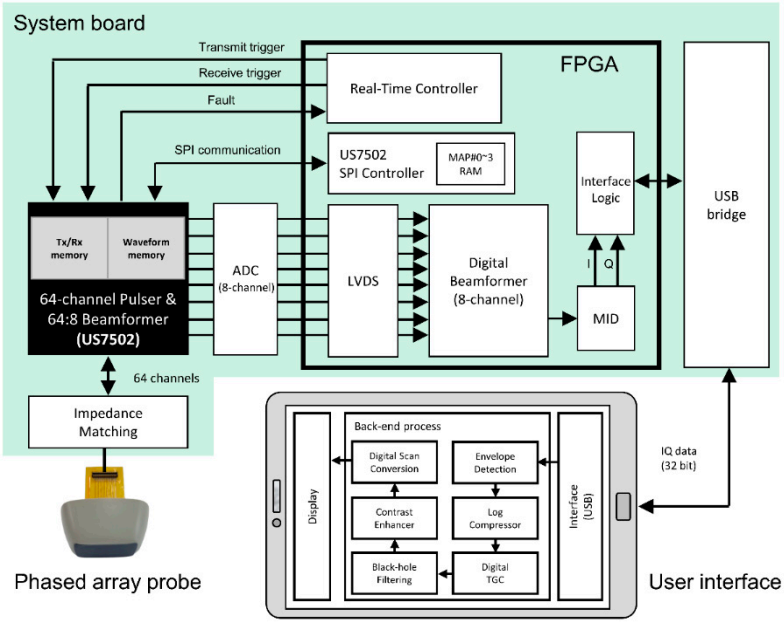


**Figure 5.** Functional block diagram of the implemented system consisting of four major ICs – two AFE ICs for analog beamforming and sampling (US7502 and AFE5801), one FPGA (Artix-7 XC7A200T), and a MCU (CYUSB3014-BZXI) for USB interface.

A custom one-dimensional 64-element phased array was used in this study, but there is no limitation in the number of channels or the type of transducers to utilize our approach. As shown in Figure 6, each channel of the analog beamformer in the US7502 has 68 taps with 20 ns of a tap charging time ($T_s$), as the clock rate of the overall system was at 50 MHz. In other words, incoming pre-beamformed analog RF signals in each channel can be continuously stored along the 68 analog FIFO taps at every 20 ns. Write control signals (WR0 to WR67) indicate serial charging of each capacitor in the 68 taps from Tap-0 to Tab-67 per channel, as shown in Figure 6. Here, for more precise beamforming, storing the signals in the neighboring taps can be overlapped with a 5-ns time step, which is referred to as a delay advance. The maximum number of this delay advance events is limited to 255 in the US7502 IC for entire firing, and the next delay advance from the prior event can happen in $8T_s$, $16T_s$, $64T_s$, $256T_s$, and $1024T_s$. The delay advance timing steps and the number of delay advance events are all specified by the IC manufacturer. After storing the analog signals correctly in the relevant tabs in the analog FIFO with appropriate beamforming delays, reading and summing operations are conducted simultaneously at every 20 ns, which finally produces partially beamformed 8-channel analog data.

Preprints (www.preprints.org) | NOT PEER-REVIEWED | Posted: 23 October 2023 doi:10.20944/preprints202310.1453.v1



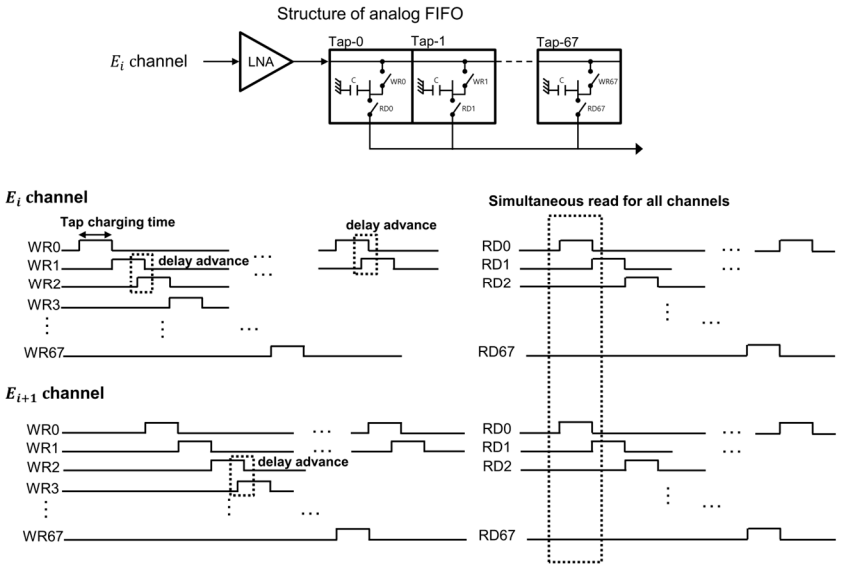


**Figure 6.** Analog FIFO structure with 68 taps and associated write/read timings in each channel. WR0 to WR67 control signals are to store the analog data into the corresponding cell of the analog FIFO in each channel. $E_i$ and $E_{i+1}$ channels in the figure mean that the different positions of the array elements induce delayed write timings. Writing receiving analog signals between cells (or taps) can be overlapped by the delay advance time. Read-out operations with RD0 to RD67 control signals are consecutively done along the cell.

### *2.4. Phantom Imaging Experiments*

A custom-made 64-element phased array transducer with a 0.24-mm pitch (i.e., element spacing), elevationally focused at 80 mm was used to verify the implemented system. A single cycle ultrasound pulse at a center frequency of 3.2 MHz was induced to the array transducer for imaging a commercial tissue mimicking phantom with cysts and point targets (Model 054GS, Mirion Technologies Inc., Georgia, USA).

To assess the imaging capabilities of the system, a signal-to-noise ratio (SNR) and a contrast-to-noise ratio (CNR), and lateral beam widths at half maximum of the signal were measured on pin and cyst targets of the phantom, respectively. SNR and CNR values were evaluated by following equations [29, 30]:

$$SNR = 20log_{10}\frac{|\mu_s|}{|\mu_n|} \tag{3}$$

$$CNR = 20log_{10}\frac{|\mu_s - \mu_b|}{|\sigma_s^2 + \sigma_b^2|} \tag{4}$$

where $\mu_s$ and $\mu_n$ in Equation (3) are the averaged signals on the point target and surrounding speckle noise region, respectively. $\mu_s$ and $\mu_b$ in Equation (4) are the averaged signals from the foreground and the background regions of cysts in the phantom, respectively. $\sigma_s$ and $\sigma_b$ are the standard deviations evaluated from the same regions, respectively.

Preprints (www.preprints.org) | NOT PEER-REVIEWED | Posted: 23 October 2023 doi:10.20944/preprints202310.1453.v1



## 3. Results and Discussion

### *3.1. Imaging Results from a Phantom with the Integrated System*

The integrated system with a power module connected to the bottom of the main system board is shown in Figure 7. The power module, which is not covered in this paper, is to provide stable high voltage sources of ultrasound pulsers for transmission in the AFE (i.e., US7502 IC) and several low voltage sources for operating two AFE ICs, a FPGA, a MCU and other peripheral ICs and components in the system board. The system clock rate for the FPGA and the AFE ADCs was at 50 MHz and another clock rate of 200 MHz was also used for precise delay advancing in the analog partial beamformer IC, which resulted in a 20-ns tap charging time and a 5-ns delay advance time, respectively, as described in the previous section.

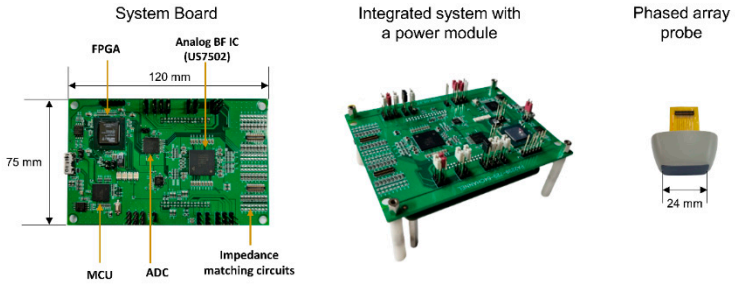


**Figure 7.** Implemented systems with four major ICs (a FPGA, a MCU, and two AFE ICs) for analog-digital hybrid beamforming and a custom 64-element phased-array used in this study. The main system is built in a printed circuit board with a dimension of 74 mm by 120 mm, whose power sources are supplied by the power module attached to the bottom of the main system board. A customized 64-element phased array transducer can be connected to the system board with impedance matching circuits in-between.

For B-mode ultrasound imaging demonstration, a single-cycle pulse with a 3.2-MHz center frequency was applied to a custom-made phased array transducer with 64 elements. The elevational focus of the probe was at 80 mm. The acoustic transmit focus was electrically created at a 60-mm depth with a total of 128 scanlines. The field of view of the image was created with –45° to +45° of scanning angles. Analog partial beamformed data (8 channel data form 64 channel inputs) from the US7520 AFE IC was transferred to the FPGA for the remaining digital beamforming after digitization by the ADCs in the AFE5801 IC. Post-beamformed IQ data then was processed in the FPGA, which was transferred to the host tablet device for further signal and imaging processing before displaying the image in real-time. The final B-mode image as shown in Figure 8 was captured from the host tablet and visualized with MATLAB software offline.

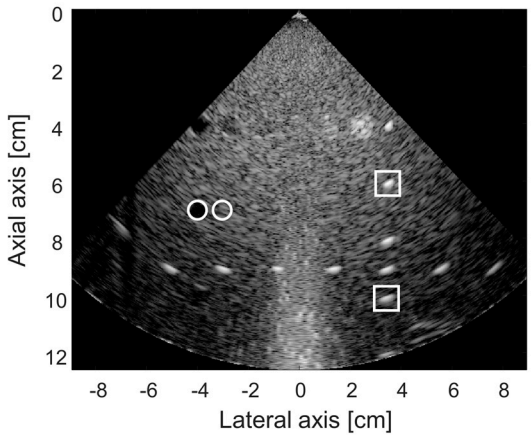

Preprints (www.preprints.org) | NOT PEER-REVIEWED | Posted: 23 October 2023 doi:10.20944/preprints202310.1453.v1



**Figure 8.** Reconstructed B-mode image with a 12-cm view depth obtained from the tissue mimicking phantom using the implemented system in this study. White circles and rectangles in the image are respectively used for CNR and SNR values. The CNR value measured from the cystic target and the corresponding background was 3.5 dB and the SNR values measured at two pin targets with different depths are 27.6 dB and 35.6 dB, respectively.

The SNR values from two pin targets (white boxes in Figure 8) were evaluated. The SNR value of the pin target located near the acoustic focus was 35.6 dB and that of the deeper target was 27.6 dB, respectively. From these two pin targets, we also measured the lateral beam widths, which were 4.1 mm and 5.1 mm, respectively. The CNR value from the hypoechoic cyst and nearby background (white circles in Figure 8) was 3.5 dB. In Figure 8, the white noise signals at the middle bottom of the image is found, which was introduced when the delays

*3.2. Practical Considerations in Analog Beamforming*

Each analog FIFO per receiving channel for partial analog beamforming in the US7502 IC has 68 taps. As 8-to-1 partial beamforming is conducted in this study, we need to consider whether all delayed signals coming into each subgroup of 8 channels can be reliably stored within a 68-tap length under the given imaging condition. In other words, a time difference between the maximum and minimum delays calculated in each subgroup elements for any imaging point for beamforming should satisfy the Equation (2). As the tap charging time $T_s$ of our system is 20 ns and each channel has 68 taps in the analog FIFO, aa maximally allowed time delay difference between channels in each subgroup would be 1,360 ns (= 68 taps × 20 ns). Thus, when the steering angle becomes large for phased array imaging, a delay difference within the 8-channel group may exceed 1,360 ns, which needs to be avoided for reliable beamforming. For example, when $\theta$ = 0°, $\varphi$ = –45°, and $R$ = 5 mm, the time delays for the first and eighth elements of the array used in this study are 9,087 ns and 7,570 ns from Equation (1), which means that this imaging condition makes the delay difference longer than 1,360 ns and this case cannot be supported for beamforming with our system.

From the worst-case analysis with our system specifications, we found that 93 taps and 366 delay advances are required for sector format imaging of a 16-cm depth, which is clearly beyond the system capability; the number of taps and the maximum number of delay advances in the US7502 IC are required to be less than or equal to 68 and 255, respectively. Figure 9 shows the maximum delay differences along the depth in the first-grouped elements (i.e., the first to eighth elements) in the array when the scanline is maximally steered at –45°. As indicated by the 1,360-ns line (a red dotted line) in Figure 9, the imaging samples from 0 mm to 6 mm cannot be correctly beamformed. Thus, based on this analysis, near field data by 6 mm was ignored to avoid missing signals during the partial analog beamforming process, which was applied to reconstruct the final image presented in Figure 8.

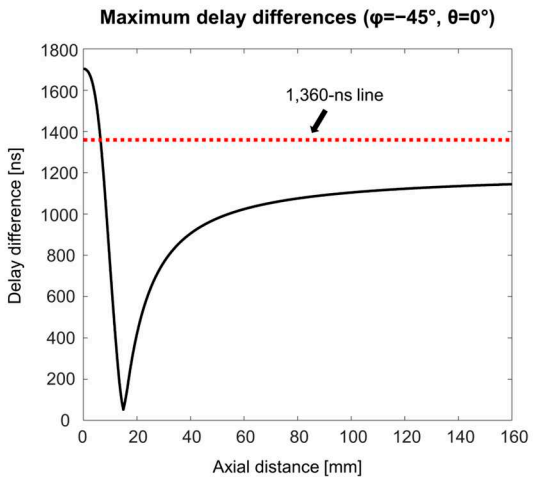

 doi:10.20944/preprints202310.1453.v1



**Figure 9.** Maximum delay differences over the axial distance for the first-grouped elements (i.e., from element 1 to element 8) with –45° of a steering angle $\varphi$ in the 1-D phased array, which demonstrates that the near field signals by about a 6-mm depth cannot be correctly beamformed with these imaging conditions, as the time delay difference exceeds the system limit (i.e., 1,360 ns).

## 4. Conclusions

This study revisited the general structures of analog and digital beamformers and compared their advantages and disadvantages in ultrasound beamforming. To mitigate their respective limitations, we have suggested their combined approach, referred to as analog-digital hybrid beamforming, potentially useful for the efficient design of massive channel ultrasound systems. We designed and demonstrated the imaging system with the reduced resources, capable of 64-channel partial analog-digital hybrid beamforming, which can be used for wearable and POCUS applications and extended to the greater number of channels for 3-D imaging applications.

**Author Contributions:** Conceptualization, H.Y. and T.S.; methodology, H.Y. and J.K.; software, J.K.; validation, H.Y., J.K. and T.S.; formal analysis, T.S.; investigation, H.Y.; resources, J.K.; data curation, H.Y.; writing—original draft preparation, H.Y.; writing—review and editing, T.S.; visualization, J.K.; supervision, T.S.; project administration, J.K.; funding acquisition, H.Y. and T.S. All authors have read and agreed to the published version of the manuscript.

**Funding:** This work was supported by the Institute of Information & communications Technology Planning & Evaluation (IITP) grant funded by the Korea government (MSIT) (No. 2022-0-00101, Development of an intelligent HIFU therapy system using highly functional real-time image guide and therapeutic effect monitoring based on ICT fusion ) and by the Technology Innovation Program (No. 20022442, Development of integrated module for osteoarthritis medical imaging and treatment using piezoelectric single crystal) funded By the Ministry of Trade, Industry & Energy (MOTIE, Korea).

**Data Availability Statement:** Data used in this study is not available.

**Acknowledgments:** Heechul Yoon and Junseung Kim equally contributed to this work.

**Conflicts of Interest:** The authors declare no conflict of interest.

## References

1. Torres-Macho J, Aro T, Bruckner I, Cogliati C, Gilja OH, Gurghean A, et al. Point-of-care ultrasound in internal medicine: A position paper by the ultrasound working group of the European federation of internal medicine. European Journal of Internal Medicine. 2020;73:67-71. doi: https://doi.org/10.1016/j.ejim.2019.11.016.
2. Hu H, Huang H, Li M, Gao X, Yin L, Qi R, et al. A wearable cardiac ultrasound imager. Nature. 2023;613(7945):667-75. doi: 10.1038/s41586-022-05498-z.
3. Catalano O, Fusco R, De Muzio F, Simonetti I, Palumbo P, Bruno F, et al. Recent Advances in Ultrasound Breast Imaging: From Industry to Clinical Practice. Diagnostics. 2023;13(5):980.
4. Park B, Kim C, Kim J. Recent Advances in Ultrasound and Photoacoustic Analysis for Thyroid Cancer Diagnosis. Advanced Physics Research. 2023;2(4):2200070. doi: https://doi.org/10.1002/apxr.202200070.
5. Yoon H, Zhu YI, Yarmoska SK, Emelianov SY. Design and Demonstration of a Configurable Imaging Platform for Combined Laser, Ultrasound, and Elasticity Imaging. IEEE Transactions on Medical Imaging. 2018:1-. doi: 10.1109/TMI.2018.2889736.
6. Millington SJ, Arntfield RT, Koenig SJ, Mayo PH, Vieillard-Baron A. Ten Influential Point-of-Care Ultrasound Papers: 2022 in Review. Journal of Intensive Care Medicine. 2023;38(6):566-70. doi: 10.1177/08850666231166898.
7. Hasegawa H. Advances in ultrasonography: image formation and quality assessment. Journal of Medical Ultrasonics. 2021;48(4):377-89. doi: 10.1007/s10396-021-01140-z.
8. Tufano A, Antonelli L, Di Pierro GB, Flammia RS, Minelli R, Anceschi U, et al. Diagnostic Performance of Contrast-Enhanced Ultrasound in the Evaluation of Small Renal Masses: A Systematic Review and Meta-Analysis. Diagnostics. 2022;12(10):2310.
9. Errico C, Pierre J, Pezet S, Desailly Y, Lenkei Z, Couture O, Tanter M. Ultrafast ultrasound localization microscopy for deep super-resolution vascular imaging. Nature. 2015;527(7579):499-502. doi: 10.1038/nature16066. http://www.nature.com/nature/journal/v527/n7579/abs/nature16066.html#supplementary-information.

10. Perrot V, Polichetti M, Varray F, Garcia D. So you think you can DAS? A viewpoint on delay-and-sum beamforming. Ultrasonics. 2021;111:106309. doi: https://doi.org/10.1016/j.ultras.2020.106309.
11. Steinberg BD. Digital beamforming in ultrasound. IEEE Transactions on Ultrasonics, Ferroelectrics, and Frequency Control. 1992;39(6):716-21. doi: 10.1109/58.165556.
12. Song TK, Park SB. A new digital phased array system for dynamic focusing and steering with reduced sampling rate. Ultrasonic Imaging. 1990;12(1):1-16. doi: https://doi.org/10.1016/0161-7346(90)90217-L.
13. Jensen JA, Nikolov SI, Gammelmark KL, Pedersen MH. Synthetic aperture ultrasound imaging. Ultrasonics. 2006;44 Suppl 1:e5-15. doi: 10.1016/j.ultras.2006.07.017.
14. Kim C, Yoon C, Park JH, Lee Y, Kim WH, Chang JM, et al. Evaluation of Ultrasound Synthetic Aperture Imaging Using Bidirectional Pixel-Based Focusing: Preliminary Phantom and In Vivo Breast Study. IEEE Transactions on Biomedical Engineering. 2013;60(10):2716-24. doi: 10.1109/TBME.2013.2263310.
15. Chen Q, Song H, Yu J, Kim K. Current Development and Applications of Super-Resolution Ultrasound Imaging. Sensors. 2021;21(7):2417.
16. Agarwal A, Reeg J, Podkowa AS, Oelze ML. Improving Spatial Resolution Using Incoherent Subtraction of Receive Beams Having Different Apodizations. IEEE Trans Ultrason Ferroelectr Freq Control. 2019;66(1):5-17. doi: 10.1109/tuffc.2018.2876285.
17. Hu CL, Wu GZ, Chang CC, Li ML. Acoustic-Field Beamforming for Low-Power Portable Ultrasound. Ultrason Imaging. 2021;43(4):175-85. doi: 10.1177/01617346211013473.
18. Yu J, Yoon H, Khalifa YM, Emelianov SY. Design of a Volumetric Imaging Sequence Using a Vantage-256 Ultrasound Research Platform Multiplexed With a 1024-Element Fully Sampled Matrix Array. IEEE Transactions on Ultrasonics, Ferroelectrics, and Frequency Control. 2020;67(2):248-57. doi: 10.1109/TUFFC.2019.2942557.
19. Lin M, Zhang Z, Gao X, Bian Y, Wu RS, Park G, et al. A fully integrated wearable ultrasound system to monitor deep tissues in moving subjects. Nature Biotechnology. 2023. doi: 10.1038/s41587-023-01800-0.
20. Xue X, Zhang B, Moon S, Xu G-X, Huang C-C, Sharma N, Jiang X. Development of a Wearable Ultrasound Transducer for Sensing Muscle Activities in Assistive Robotics Applications. Biosensors. 2023;13(1):134.
21. Austeng A, Holm S. Sparse 2-D arrays for 3-D phased array imaging - design methods. IEEE Transactions on Ultrasonics, Ferroelectrics, and Frequency Control. 2002;49(8):1073-86. doi: 10.1109/TUFFC.2002.1026019.
22. Yoon H, Song TK. Sparse Rectangular and Spiral Array Designs for 3D Medical Ultrasound Imaging. Sensors (Basel). 2019;20(1). doi: 10.3390/s20010173.
23. Jensen JA, Schou M, Jorgensen LT, Tomov BG, Stuart MB, Traberg MS, et al. Anatomic and Functional Imaging Using Row-Column Arrays. IEEE Trans Ultrason Ferroelectr Freq Control. 2022;69(10):2722-38. doi: 10.1109/tuffc.2022.3191391.
24. Giangrossi C, Ramalli A, Dallai A, Mazierli D, Meacci V, Boni E, Tortoli P. Requirements and Hardware Limitations of High-Frame-Rate 3-D Ultrasound Imaging Systems. Applied Sciences. 2022;12(13):6562.
25. Kim JH, Song TK, Park SB. Pipeline sampled-delay focusing in ultrasound imaging systems. Ultrason Imaging. 1987;9(2):75-91. doi: 10.1177/016173468700900201.
26. Um JY, Kim YJ, Cho SE, Chae MK, Kim B, Sim JY, Park HJ. A single-chip 32-channel analog beamformer with 4-ns delay resolution and 768-ns maximum delay range for ultrasound medical imaging with a linear array transducer. IEEE Trans Biomed Circuits Syst. 2015;9(1):138-51. doi: 10.1109/tbcas.2014.2325851.
27. Mucci R. A comparison of efficient beamforming algorithms. IEEE Transactions on Acoustics, Speech, and Signal Processing. 1984;32(3):548-58. doi: 10.1109/TASSP.1984.1164359.
28. Um JY, Kim YJ, Cho SE, Chae MK, Song J, Kim B, et al. An Analog-Digital Hybrid RX Beamformer Chip With Non-Uniform Sampling for Ultrasound Medical Imaging With 2D CMUT Array. IEEE Transactions on Biomedical Circuits and Systems. 2014;8(6):799-809. doi: 10.1109/TBCAS.2014.2375958.
29. Rodriguez-Molares A, Rindal OMH, D'Hooge J, Masoy SE, Austeng A, Lediju Bell MA, Torp H. The Generalized Contrast-to-Noise Ratio: A Formal Definition for Lesion Detectability. IEEE Trans Ultrason Ferroelectr Freq Control. 2020;67(4):745-59. doi: 10.1109/tuffc.2019.2956855.
30. Sassaroli E, Crake C, Scorza A, Kim DS, Park MA. Image quality evaluation of ultrasound imaging systems: advanced B-modes. J Appl Clin Med Phys. 2019;20(3):115-24. doi: 10.1002/acm2.12544.